PASJ: Publ. Astron. Soc. Japan **61**, S35–S53, 2009 January 30

Design and In-Orbit Performance of the Suzaku Wide-Band All-Sky Monitor

Kazutaka YAMAOKA,[1] Akira ENDO,[2] Teruaki ENOTO,[3] Yasushi FUKAZAWA,[4] Ryuji HARA,[5] Yoshitaka HANABATA,[4] Soojing HONG,[6] Tsuneyoshi KAMAE,[7] Chie KIRA,[4] Natsuki KODAKA,[2] Motohide KOKUBUN,[8] Shouta MAENO,[9] Kazuo MAKISHIMA,[3,10] Ryohei MIYAWAKI,[3] Kouichi MORIGAMI,[2] Toshio MURAKAMI,[11] Yujin E. NAKAGAWA,[10] Kazuhiro NAKAZAWA,[3] Norisuke OHMORI,[5] Masanori OHNO,[8] Kaori ONDA,[2] Goro SATO,[8] Eri SONODA,[5] Satoshi SUGITA,[1,10] Masanobu SUZUKI,[2] Motoko SUZUKI,[12] Hiroyasu TAJIMA,[7] Tadayuki TAKAHASHI,[8] Takuya TAKAHASHI,[4] Hiroki TANAKA,[5] Tohru TAMAGAWA,[10] Makoto S. TASHIRO,[2] Yukikatsu TERADA,[2] Takeshi UEHARA,[4] Yuji URATA,[2,13] Makoto YAMAUCHI,[5] Atsumasa YOSHIDA,[1] Kevin HURLEY,[14] Valentin PAL'SHIN,[15] Takanori SAKAMOTO,[16,17] and Jay CUMMINGS[16,18]

[1] *Department of Physics and Mathematics, Aoyama Gakuin University, 5-10-1 Fuchinobe, Sagamihara, Kanagawa 229-8558*
yamaoka@phys.aoyama.ac.jp
[2] *Department of Physics, Saitama University, 255 Shimo-Okubo, Sakura-ku, Saitama-shi, Saitama 338-8570*
[3] *Department of Physics, University of Tokyo, 7-3-1 Hongo, Bunkyo-ku, Tokyo 113-0033*
[4] *Department of Physics, Hiroshima University, 1-3-1 Kagamiyama, Higashi-Hiroshima, Hiroshima 739-8526*
[5] *Department of Applied Physics, University of Miyazaki, 1-1 Gakuen Kibanadai-nishi, Miyazaki-shi, Miyazaki 889-2192*
[6] *College of Science and Technology, Nihon University, 7-24-1 Narashinodai, Funabashi-shi, Chiba 274-8501*
[7] *Stanford Linear Accelerator Center (SLAC), 2575 Sand Hill Road, Menlo Park, CA 94025, USA*
[8] *Department of High Energy Astrophysics, Institute of Space and Astronautical Science Aerospace Exploration Agency (ISAS/JAXA), 3-1-1 Yoshinodai, Sagamihara, Kanagawa 229-8510*
[9] *Nishi-Harima Astronomical Observatory, 407-2 Sayo-chou, Sayo-gun, Hyougo 679-5313*
[10] *Makishima Cosmic Radiation Laboratory, The Institute of Physical and Chemical Research (RIKEN), 2-1 Hirosawa, Wako, Saitama 351-0198*
[11] *Department of Physics, Kanazawa University, Kadoma-cho, Kanazawa, Ishikawa 920-1192*
[12] *ISS Science Project team, Institute of Space and Astronautical Science Aerospace Exploration Agency (ISAS/JAXA), 2-1-1 Sengen, Tsukuba, Ibaraki 305-8505*
[13] *Academia Sinica Institute of Astronomy and Astrophysics, Taipei 106, Taiwan, Republic of China*
[14] *University of California, Berkeley, Space Sciences Laboratory, 7 Gauss Way, Berkeley, CA 94720-7450, USA*
[15] *Laboratory for Experimental Astrophysics, Ioffe Physico-Technical Institute, 26 Polytekhnicheskaya, St Petersburg 194021, Russian Federation*
[16] *NASA Goddard Space Flight Center, Greenbelt, MD 20771, USA*
[17] *Oak Ridge Associated Universities, P.O. Box 117, Oak Ridge, TN 37831-0117, USA*
[18] *Joint Center for Astrophysics, University of Maryland, Baltimore Country, 1000 Hilltop Circle, Baltimore, MD 21250, USA*

(Received 2008 July 31; accepted 2008 November 1)

Abstract

The Suzaku Wide-band All-sky Monitor (WAM) consists of thick BGO anti-coincidence shields of the Hard X-ray Detectors (HXD). It views about half of the sky and has a geometrical area of 800 cm^2 per side and an effective area of 400 cm^2, even at 1 MeV. Hence, the WAM can provide unique opportunities to detect high-energy emission from GRBs and solar flares in the sub-MeV to MeV range. The WAM has detected more than 400 GRBs and 100 solar flares since its launch. This paper describes the in-flight performance of the HXD/WAM during the initial two years of operations, including the in-flight energy response, spectral and timing capabilities, and in-orbit background.

Key words: gamma rays: observations — instrumentation: detectors

1. Introduction

The hard X-ray sky (> 10 keV) is very violent and variable. Non-thermal phenomena related to particle acceleration and explosions are dominant at this wavelength, while in the soft X-ray range (< 10 keV) thermal radiation processes are observed at various sites, such as supernova remnants, clusters of galaxies, and X-ray binaries. There are many bright sources, which range from the solar-system to cosmological distances in this energy range: Gamma-ray bursts (GRBs), soft gamma-ray repeaters (SGRs), bursting pulsars such as GRO J1744−28 (Paciesas et al. 1996), outbursts of black-hole and neutron star binaries, solar flares, and terrestrial gamma-ray flashes (TGFs: Fishman et al. 1994). All of these phenomena can instantaneously brighten to intensites greater than Crab Nebula, and have been discovered and observed with various wide-field instruments since the begining of X-ray astronomy. The Burst and Transient Source Experiment (BATSE) aboard the Compton Gamma-ray Observatory (CGRO) was the largest all-sky monitor. It made numerous important discoveries in these

Table 1. List of abbedreations.

AE	Analog Electronics (in the Suzaku Hard X-ray Detector).
BST data	Gamma-burst data.
CFRP	Carbon-Fiber Reinforced Plastic.
DE	Digital Electronics (in the Suzaku Hard X-ray Detector).
FOV	Field-Of-View.
GRB	Gamma-Ray Burst.
HXD	Hard X-ray Detector.
IPN	Inter-Planetary Network.
LD	Lower Discriminator.
PMT	Photo-Multiplier Tube.
PH	Pulse Height.
RBM	Radiation Belt Monitor.
RI	Radioisotope.
SAA	South Atlantic Anomaly.
SGR	Soft Gamma Repeater.
TPU	Transient Processing Unit (= WAM analog electronics).
TRN data	Transient data.
TH	Time History.
UD	Upper Discriminator.
WAM	Wide-band All-sky Monitor.
XRS	X-Ray Spectrometer.
XRT	X-Ray Telescope onboard Suzaku.

areas, such as the uniform GRB spatial distribution. Currently, Swift is the main mission in this field, with its Burst Alert Telescope (BAT: Gehrels et al. 2004), dedicated to the prompt localization of GRBs. Our understanding of the hard X-ray region is constantly improving, yet there is still room for new and unexpected discoveries.

Suzaku is the fifth Japanese X-ray astronomical satellite, following Hakucho, Tenma, Ginga, and ASCA (Mitsuda et al. 2007). It was launched on 2005 July 10 by a M-V rocket at the Uchinoura Space Center (USC) in Japan, and placed into a near-Earth orbit with an altitude of 570 km and an inclination angle of 31°. Suzaku carries three narrow-field of view scientific instruments: an X-ray micro-calorimeter array [X-ray Spectrometer (XRS): Kelley et al. 2007], X-ray CCD cameras [X-ray Imaging Spectrometer (XIS): Koyama et al. 2007], and a Hard X-ray Detector (HXD: Takahashi et al. 2007; Kokubun et al. 2007). The XRS is not operational due to an accident with a liquid-He dewar, but the XIS and HXD have been operating nominally. With these two instruments, Suzaku covers a very wide energy range, 0.2–600 keV, with high sensitivity. In addition to these narrow-field instruments, Suzaku has an all-sky monitor with broad-band coverage from 50 to 5000 keV, a wide-band all-sky monitor (WAM: Yamaoka et al. 2005, 2006). It utilizes the lateral BGO anti-coincidence shields of the HXD, which are similar to the INTEGRAL SPI-ACS (von Kienlin et al. 2003) and the Beppo-SAX GRBM (Feroci et al. 1997). Since its activation, the WAM has detected bright hard X-ray and soft gamma-ray sources, such as gamma-ray bursts (GRBs), soft gamma-ray repeaters (SGRs), solar flares, hard X-ray transients, and others. Thus, we can say that the WAM has established itself firmly as the fourth instrument aboard Suzaku, and it will continue to study non-thermal phenomena in the hard X-ray range.

In this paper, we describe the design and in-orbit performance of the Suzaku WAM based on the first two years of operation. In section 2, we present the overall design of the Suzaku WAM. In sections 3, 4, and 5, in-flight operation, in-orbit background, and calibrations are presented. Based on GRB observations, we discuss the performance for GRB detections in sections 6 and 7. Finally, we present some results on other astronomical sources.

2. Suzaku Wide-Band All-Sky Monitor (WAM)

2.1. Concept of the WAM

The HXD is a new type of detector with an extremely low background, made possible by tight active shielding and a very limited field of view (FOV). It is composed of 16 identical BGO / GSO well-type phoswich counters (Well) installed with Si-PIN diodes, and further surrounded on four sides by 20 BGO anti-coincidence detectors (figure 1). The primary role of the lateral BGO crystals is to serve as active shields for the HXD main detectors (Si PIN diodes and GSO). In addition, they have a large geometrical area (800 cm^2 per side), and also present a large effective area for gamma rays owing to their thick high-Z materials ($Z_{\rm eff} = 71$ for BGO). Figure 2 shows the effective area of each wall for normal incidence in comparison with other previous or current GRB instruments, including CGRO / BATSE, Fermi / GBM, and Swift / BAT. The WAM achieves a larger effective area in the MeV range than any of these detectors. It has an uncollimated field of view, since it is positioned at the side of the HXD, and a relatively unobstructed field of view thanks to the HXD position on the Suzaku satellite. It sits apart from the X-ray telescope (XRT: Serlemitsos et al. 2007) and extensible optical bench (EOB) (see figure 3) to maintain its FOV. Utilizing these two advantages, we have

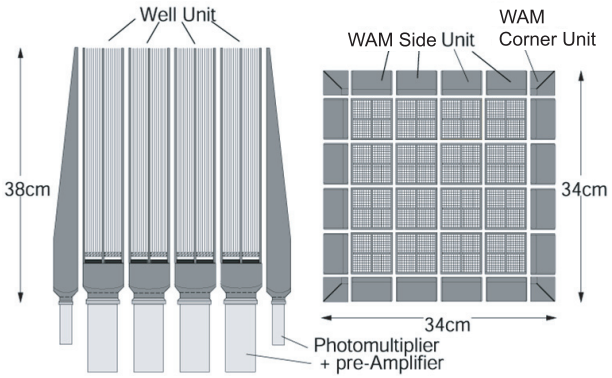

Fig. 1. Schematic view of the Hard X-ray Detector. Left panel: Cross-sectional view. Right panel: Top view. The WAM is a subsystem of the HXD which consists of the surrounding 20 BGO anti-coincidence shields.

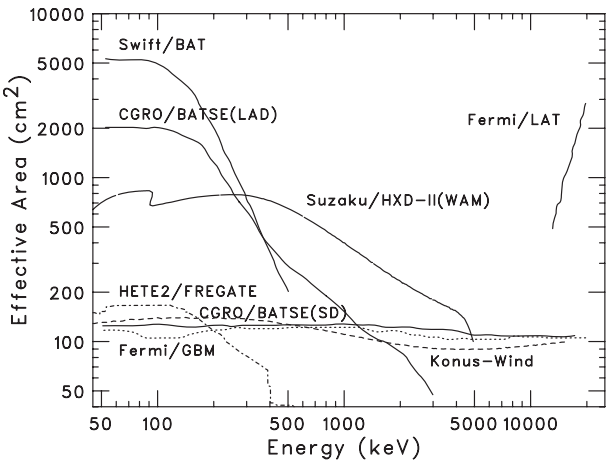

Fig. 2. On-axis effective area of the Suzaku WAM in comparison with previous and current GRB detectors. Some of them are shown not as a solid line, but rather a dotted line for Fermi / GBM, a dashed line for Konus-Wind, and a dot-dashed line for HETE-2 / FREGATE. The Suzaku WAM has a very large effective area 400 cm^2 in the MeV range.

designed this shield as a wide-band all-sky monitor for hard X-ray transients, such as GRBs and bright hard X-ray sources using the Earth occultation method (Harmon et al. 2002). The characteristics of the WAM are summarized in table 2.

2.2. *Overview of the WAM*

The general WAM signal processing flow is shown in figure 2 of Takahashi et al. (2007). When a hard X-ray photon interacts with the WAM sensors, the green-blue light (peaked at 480 nm) produced in the scintillators is converted into electrical signals in the photomultiplier tubes and pre-amplifiers of the sensors. Through filters and amplifiers in the analog electronics (HXD-AE: subsection 2.4), their pulse height, corresponding to the photon energy, is digitized by Analog to Digital Converters (ADC). The ADC and scaler information are integrated for a fixed time as histogram data (TRN data and BST data: subsection 2.4). These WAM data are compressed and packeted by digital electronics (HXD-DE: subsection 2.5), and sent as telemetry to the digital processor (DP). The data are

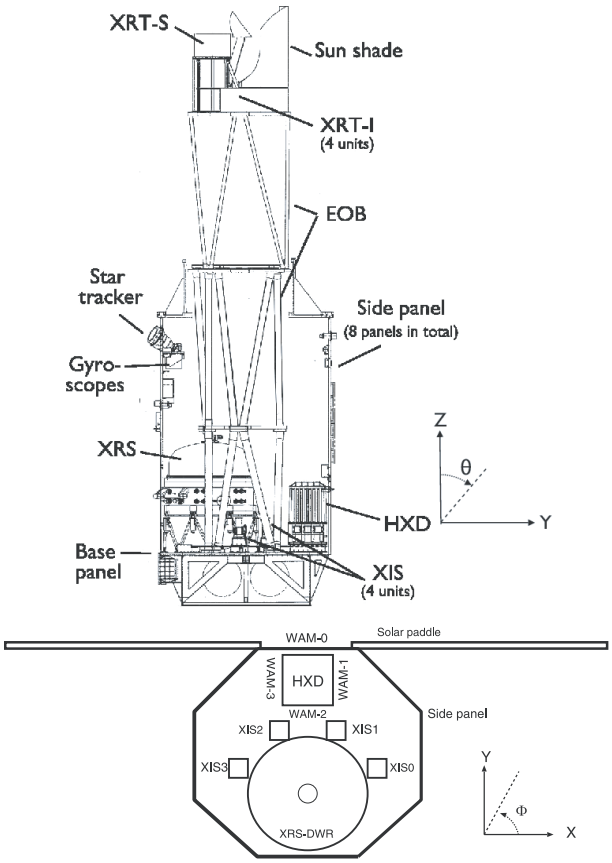

Fig. 3. Suzaku configuration. Upper panel: Cross-sectional view. Lower panel: Top view. The HXD / WAM is installed opposite to the XRS and apart from the XRT to maintain an unobstucted HXD FOV.

temporarily accumulated in the data recorder (DR), which can hold 6 Gbytes. The Suzaku satellite passes over the Uchinoura Space Center (USC) in Japan 5 or 6 times per day. The satellite is in contact with the ground-station at USC for about 10 min out of every 96 min for each viewing period.[1] During this short period, the operational commands (OPs) are up-linked, while the WAM data in the DR are down-linked. The typical WAM data volume for one day is about 50 MBytes.

2.3. *Detectors*

The WAM consists of four identical walls, which are numbered 0 to 3. The elevation and the azimuth angles (θ, ϕ) for the WAM are defined in figure 3. WAM 0 and WAM 1 face the positive direction of the satellite Y- and X-axes, respectively. WAM 0 is located near the solar paddle ($\phi = 90°$), which is sometimes affected by strong solar flares. WAM 2 is in front of the XRS dewar ($\phi = 270°$), which results in heavy absorption of the incident gamma-rays.

Each WAM wall is composed of two different types of BGO crystals: four Side units and one Corner unit located at the corner of the HXD. The Corner units have a thinner structure than the Side units. Each WAM unit consists of a BGO crystal, a photomultiplier tube (PMT), a high-voltage

[1] The operation is resumed every Sunday, so the data down-link is also stopped.

Table 2. Characteristics of the Suzaku wide-band all-sky monitor.

Sensors	20 BGO crystals (readout by PMT)
Number of detectors	4 (referred to as WAM 0–3)
Energy range	50–5000 keV (55 energy channels)
Geometrical area	800 cm^2 per side
Effective area@1 MeV	400 cm^2 per side
Energy resolution@662 keV	$\sim$30%
Field of view	$\sim 2\pi$
Time resolution	1/64 s during 64 s of the burst (BST data)*
	continuous 1 s (TRN data)
Telemetry rate	5 kbps
Response time to GRBs	within a day (no alerts)
GRB localization capability	5°–10° using the WAM alone, $< 1°$ by the IPN

* Since 2006 March 20. 1/32 s during 128 s of the burst before this date.

divider, and a pre-amplifier. The BGO crystal has a wedge-like shape with a size of 38 cm × 5.7 cm and an average thickness of 2.6 cm. This shape is determined so that it produces almost the same path lengths as viewed from the PIN and GSO in the Well units. In sensor production, we painted $BaSO_4$ with epoxy-glue on the crystal surface as the scintillation light reflector, then attached a Reny 1022F block and a thin CFRP (Carbon Fiber Reinforced Plastic) plate at the top and bottom of each crystal to protect the sensor from vibration during launch (figure 4). Each unit consists of two BGO blocks, called the top and bottom part, glued together at the middle and optically coupled to a PMT with a diameter of 1–1/8″ (Hamamatsu R3998-01 MOD: modifed version for vibration and shock) and viewed by it (figure 5). This PMT has a high quantum efficiency ($\sim$25%) at the peak wavelength ($\sim$480 nm), which the BGO scintillator emits. The optical coupling between the BGO and the PMT is transparent silicon rubber (KE 108: Shinetsu Chemical Ltd.). The high voltages on the PMTs are designed to provide for one WAM wall, i.e., 5 WAM units simultaneously. Two-stage emitter followers were used for the pre-amplifier because of their low power (3.8 mW per unit). Their signals are read out through 4 m co-axial cables by independent analog electronics boards (AE-TPU 0, 1, 2 to 3) on the panel.

2.4. *Analog Electronics (AE-TPU)*

The role of the analog electronics is to process the signals for the 20 WAM sensors and to produce two types of digitized histogram data, which are sent to the digital electronics. Figure 6 shows the overall design of the analog electronics for the WAM (AE-TPU: Transient data Processing Unit). It consists of analog and digital logic components. The Analog parts consist of the discrete electrical components, while almost all of the logic blocks are radiation-hardened Actel FPGA (RT1280A-1CQ172E).

The pre-amplifier outputs from the WAM sensors are transfered into the AE-TPU. Each gain is adjusted at the 8-bit gain-controlled amplifier. Its output is divided into two components: lower-level discriminator (LD) for the veto signals to the HXD PIN/GSO (the so-called "hit pattern") and summing amplifier for pulse-height analysis. Thus, we can reduce the PIN/GSO background using the hit information of their event data in-flight or on the ground.

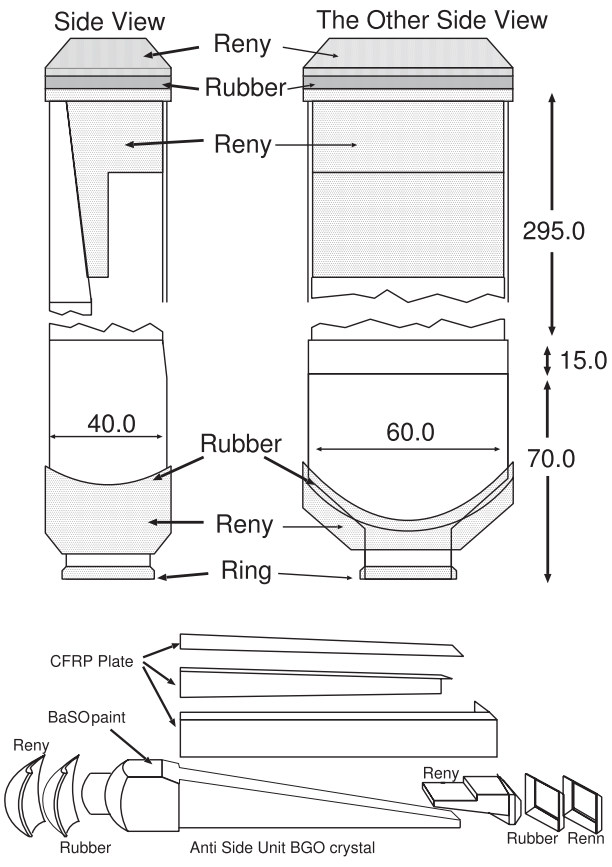

Fig. 4. Assembly of the WAM sensor (Side Unit). The BGO crystals were protected from vibrations and shocks during launch by attached plastics such as CFRP, Reny, and reflector $BaSO_4$.

In addition, the summing amplifier can select signals from any of the five units by an analog switch. The pulse height of the summed signal is digitized by a 6-bit flash ADC with one overflow bit (Harris CA3306) at the timing of the peak detection pulse triggered by the lower discriminator for summed events (Sum LD). The 65 pulse-height (PH) channels, i.e., 64 plus one overflow bit, are bit-compressed into 55 channels, as shown in table 3, and the spectrum is accumulated over

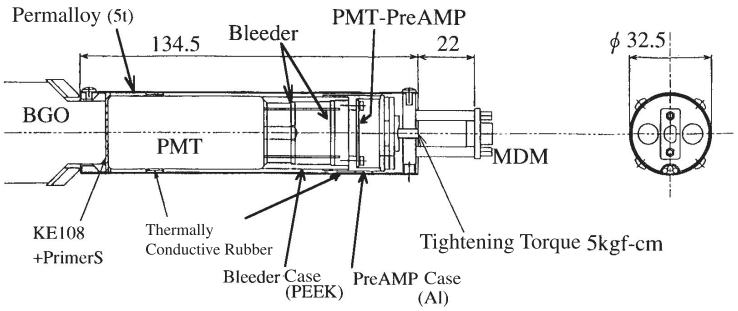

Fig. 5. Assembly of the WAM PMTs and front-end electronics (bleeders and pre-amplifiers). Left panel: Side view. Right panel: Bottom view.

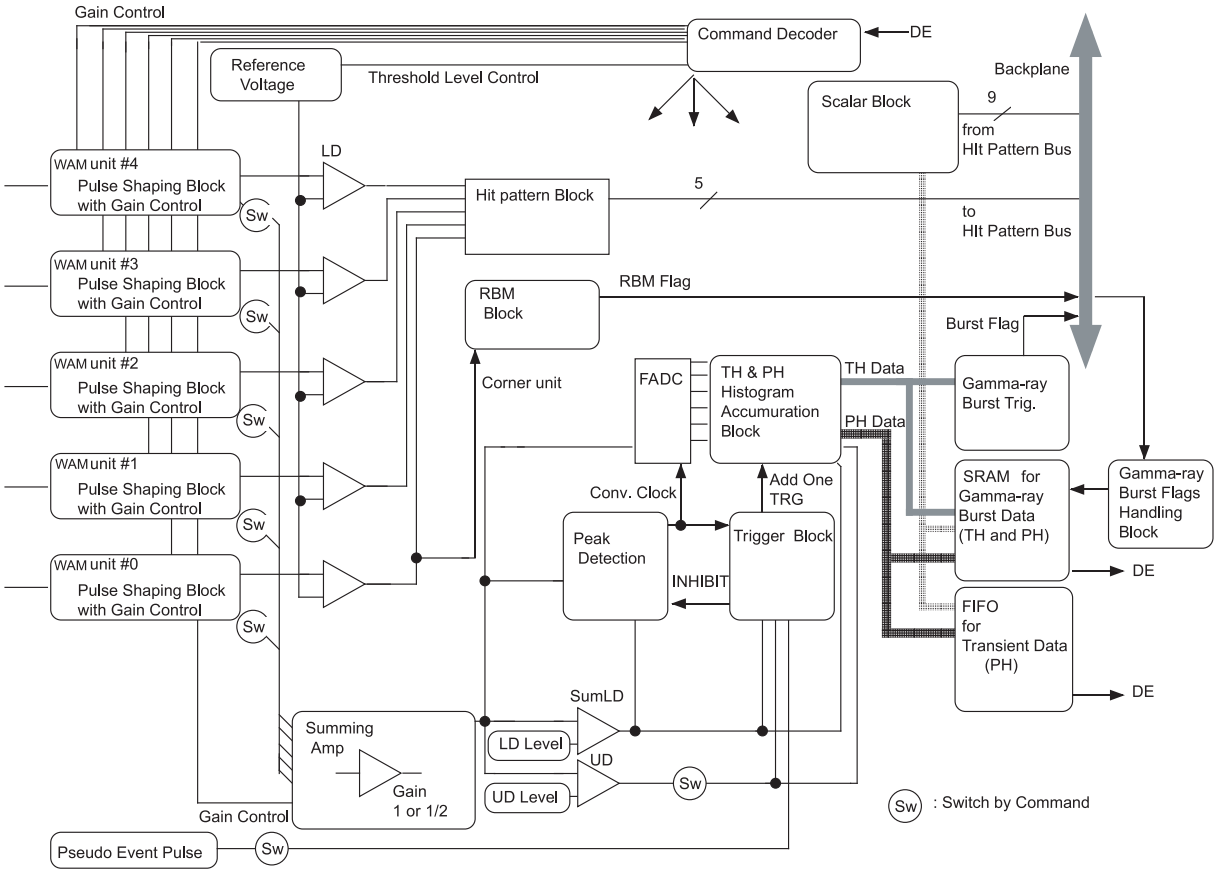

Fig. 6. Overall signal-processing scheme of one WAM analog electronics unit (AE-TPU). The four identical boards are used for WAM data processing.

a fixed time according to the time mode (0.5, 1, 2, or 4 s). If the pulse height exceeds the upper discriminator (UD) level of 9 V, corresponding to a photon energy of 5 MeV, event accumulation is inhibited for 25.6 μs from the initial trigger. The deadtime is measured by a deadtime counter, which counts the deadtime clock with a frequency of 7.8125 MHz (= a period of 12.8 μs) during the deadtime pulse.[2] The deadtime for one normal event is fixed at 12.6 μs, while the UD event is fixed at 25.6 μs, so we can also estimate the approximate deadtime using the rates of the UD and PH counters. The TPU also monitors various scaler information for each unit, such as the LD, Sum LD, UD, and hit-signals in the 16 units of the Well detectors (Slow LD). Both the PH and scaler data are accumulated

Table 3. Bit-compression for 6-bit Flash ADC channels.

Compressed channels	Original channels	Binning
0–47	0–47	1
48–51	48–55	2
52–53	56–63	4
54	Overflow bit	1

[2] The AE-TPU has a pseudo-event pulse for deadtime estimation in the same way as the PIN and GSO, but this method requires a longer integration time, so we do not use this for the WAM events with typically shorter durations of 1–100 s.

Table 4. Characteristics of the WAM data (TRN data and BST data).

Data	Epoch	Energy	Time resolution	Time coverage
BST	2005 Aug 22–2006 Mar 20	4 ch	1/32 s (TH)	128 s (16 s before and 112 s after the trigger)
		55 ch	1 s (PH)	
	2006 Mar 20–present	4 ch	1/64 s (TH)	64 s (8 s before and 56 s after the trigger)
		55 ch	0.5 s (PH)	
TRN	2005 Aug 22–present	55 ch	1 s (PH)	Always transferred to the telemetry every 1 s

into a 1 Kbyte FIFO, and sent as TRN data (table 4) to the DE in response to a DE request every second.

In addition, the TPU handles the high time resolution GRB data (BST data: table 4) which contain the time history (TH) data in four energy bands (table 5). It triggers in response to a sudden count rate increase over statistical background fluctuations according to the following algorithm:

$$S\Delta t - Bg\Delta t > \sigma\sqrt{Bg\Delta t}. \quad (1)$$

Here, S is the source plus background rate, Bg is the averaged background rate, which is estimated over an 8-sec integration before the trigger, Δt is the sampling time (1/4 or 1 s or both), and σ is the significance level set by command (5.7, 8.0, 11.2, or 16.0). We can choose one of the four TH bands for the sample. Once this condition in any one of the four WAMs is satisfied, the GRB flag for all of the detectors is activated, and the ring buffers (Static RAM; SRAM) are frozen after storing the data before and after a burst, and the freeze flag is activated. Data readout is initiated by a command from the DE if both the GRB trigger flag and the freeze flag are on. We nominally read out the BST data by OPs during the SAA passage ($\sim$30 min), so as not to reduce the bandwidth for other observational data transfer due to their large data (256 Kbytes = 64 Kbytes $\times$ 4 WAMs). After data readout, both flags are turned off, and the TPU trigger system can receive the next GRB trigger. The details of the burst trigger are given in table 6.

Since Suzaku is in a low-Earth orbit with an inclination angle of 31°, it crosses the South Atlantic Anomaly (SAA) ten times a day. During the SAA passage, the high voltages of all the photomultiplier tubes are reduced by OPs to protect the PMTs from damage due to a huge amount of scintillation light induced by high-energy particle interactions. The WAM works as a radiation-belt monitor (RBM) for fail-safe operation. When the counts in any of the four Corner units over 8 s increases to a certain level, the high voltages of all the 36 HXD PMTs, including the 16 Well detectors are designed to be reduced automatically. This threshold level must be set carefully so that observation time is not lost needlessly. The eight levels are selectable at 1 to 300 kHz.

2.5. *Digital Electronics and On-Board Data Reduction*

In the digital electronics (HXD-DE), all of the HXD data, including the WAM data, are collected, compressed and packeted. These are processed by one CPU 80386 at 33 MHz. The TRN data, with finite sizes (144 Kbytes for one board), are always outputted to the telemetry in response to requests of the DE every second. This means that there is a possibility that they occupy a major part of the telemetry buffer for some data rates,[3] so the time and energy information in the TRN data can be compressed by on-board software (the PI program, subsection 4.4 in Takahashi et al. 2007) to reduce the telemetry. The PI program can also determine the presence of a burst by monitoring the scaler information in the TRN data. A more flexible setting than AE-TPU can be used. We can select two energy ranges for any PH energy channels, background estimation time, and significance level, although the trigger time is fixed at the time resolution of the TRN data, nominally 1 s. The software can judge a burst using scaler data, Slow LD, from the 16 Well detectors.

No alerts or rapid responses to GRBs, such as Swift and INTEGRAL, can be generated, because there are no data-relay satellites for the Suzaku mission. For prompt notification of transient phenomena, the Suzaku WAM team is allowed to analyze the temporal data at USC for quick-look analysis and release GCN circulars and Astronomers' Telegrams about their results. If any BST data are included in the telemetry, the Suzaku USC duty scientists quickly send an e-mail alert to the WAM team and the IPN team, even if it is certain that the signal is not due to a real GRB. At this stage, the light-curve data for

Table 5. Approximate energy ranges of the Time History (TH) channels.

Energy band	Corresponding energy range*
TH 0 (PH 2–3)	50– 110 keV
TH 1 (PH 4–7)	110– 240 keV
TH 2 (PH 8–16)	240– 520 keV
TH 3 (PH 17–54)	520–5000 keV

* Note that this energy range can be changed by changing the gain of the photomultiplier tubes.

Table 6. Burst triggering for the AE–TPU and DE.

	AE–TPU	DE
Energy band	1 out of 4 TH bands	2 sets of any PH energy ranges
Sample time (Δt)	1 and/or 1/4 s	1 s
Threshold level (σ)	$16\sqrt{k/m}$ k, m = 1,2,4,8	0.25–63.75
Background Integration time	8 s (fixed)	1–16 s

[3] The data rate can be selected from the four rates (512 Kbps: Super-high, 256 Kbps: High, 128 Kbps: Medium, and 32 Kbps: Low).

Table 7. WAM operations since the Suzaku launch.

Date	Events
2005 Jul 23	HXD-DE was turned on.
2005 Jul 24	HXD-AE was turned on.
2005 Jul 25–Aug 7	High voltage operations and AE-TPU parameter adjustment.
2005 Aug 8–14	High voltage off due to the XRS accident.
2005 Aug 15–17	High voltage operations (0 V→500 V→850 V).
2005 Aug 22	GRB monitor functions and BST data readout were activated.
2005 Aug 27	RBM threshold level changed (WAM 0,1: 5→10 kHz).
2005 Sep 17	RBM threshold level changed (WAM 0,1 = 100 kHz, WAM 2,3 = 10 kHz).
2005 Oct 31	GRB trigger level changed ($8.0\sigma \rightarrow 5.7\sigma$).
2006 Mar 20	Time resolution of BST data was changed (1/32 s → 1/64 s).
2006 Jun 16	Gains of the three units (T13,14,33) were changed.
2007 Apr 12	Gains of all the units were changed.

GRBs, SGRs, and solar flares are available at the Suzaku WAM web site. After the standard pipeline processing, typically one week after an observation, the WAM TRN and BST data are available to both the PIs and the WAM team for more careful analysis. The public analysis software for the WAM data has been included as a part of the HEADAS package.

3. In-Flight Operation

3.1. Operation

WAM activation started on 2005 July 25 during the commissioning phase, together with the HXD main detector (table 7). After the DE and AE-TPU were turned on, the bias voltages (HVs) for the WAM were first activated at a reduced value of 500 V during the satellite visibility window to check the electronics. Then, the HVs were carefully raised to their nominal values of around 850 V (816, 860, 878, and 874 V for WAM 0, 1, 2, and 3, respectively). All of the HVs were temporarily turned off for safety when accidental helium evaporation from the XRS dewar occurred on August 8. The HV operations were resumed between August 15 and August 17. Since then, the values of the HVs have remained unchanged up to present time.

The parameters in the AE-TPU were set after the HVs were on. The summing amplifier was set so as to sum the signals from the four Side units, except for the Corner units, because they have different energy responses from those of the Side units. The energy scale of each unit was adjusted by gain-controlled amplifiers in the TPU, so that the ADC channel 15.5 corresponds to the 511 keV positron-electron annihilaton line, which is clearly seen due to activation of the surrounding material after SAA passages. This setting results in an enegy range of 50–5000 keV. The spectra and the gains for all 20 units have been monitored by selecting one of the five WAM units in the summing amplifiers one by one. This operation is performed daily during 10 min after the SAA passage. Figure 7 shows the histories of the 511 keV peak channels for the five units of WAM 3. The gains of all the units have been gradually decreasing at a rate of 1.9% month^{-1} since launch. We adjusted the gains of T13, T14, and T33 slighly (see the definition of the detector in Takahashi et al. 2007), which was different by 20% from those of the other units, on 2006 June 16. Furthermore,

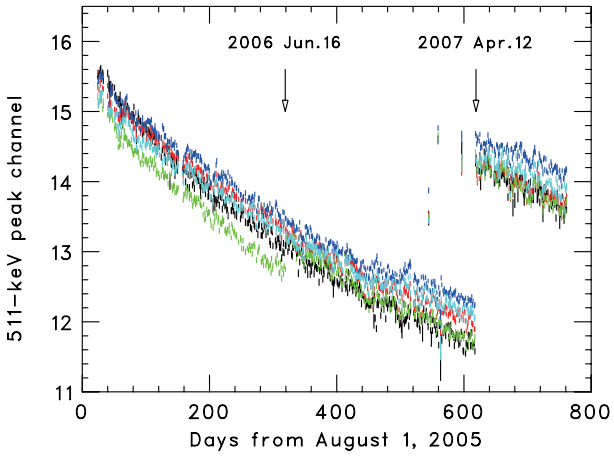

Fig. 7. Gain history of the five WAM 3 units. The 511 keV annihilation line is used for gain monitoring in the course of daily operations. The gains of all the units have gradually been decreasing with time since Suzaku launch, probably due to PMT aging. Gain change operations have been performed twice (2006 June 16 and 2007 April 17) so far.

we performed a gain-recovery operation on all of the units on 2007 April 12 to restore the original gain (channel 15.5 = 511 keV), but the gains continued to decrease after this operation. This trend is independent of the sensor temperature, indicating that it is probably due to PMT aging under the particle environment. The current gain is 20% lower than the default value, corresponding to an energy range of 60–6000 keV. The differences among the 20 units are 10% at most (figure 8). The gain variation on a daily timescale is expected from the HXD/GSO results at a few % level, due to the temperature and re-activation of high voltages after the SAA. We also confirmed this result based on both a pre-launch experiment and in-orbit measurements. The threshold levels for the LD and Sum LD were set at 128 mV and 45 mV, corresponding to photon energies of 50 keV and 30 keV, respectively.

The time resolution of the TRN and BST data, i.e., time mode, was changed on 2006 March 20 to obtain fine time resolution data for short GRBs. The TRN data were compressed

to 1 s resolution by DE onboard software to prevent telemetry saturation. The number of energy channels (55 channels) is always maintained for all of the data rates.

The RBM function was activated with the AE-TPU activations. The initial value was 5 kHz for all of the Corner units. This level is 5-times higher than the usual average rate of 900 Hz. However, the WAM often suffered from high solar activity between 2005 August 24 and September 13. The RBM flag was activated 14 times during this period, and the high voltages of all the PMTs in the HXD were automatically shut down. The HXD observation time was lost while the RBM flag was active, although the RBM functions were verified to be normal. We finally raised the threshold level up to 100 kHz for WAM 0 and 1 located at the side of the solar panel, and 10 kHz for WAM 2 and 3 at the other side starting 2005 September 17. Since then, no RBM flags have been activated by solar flares.

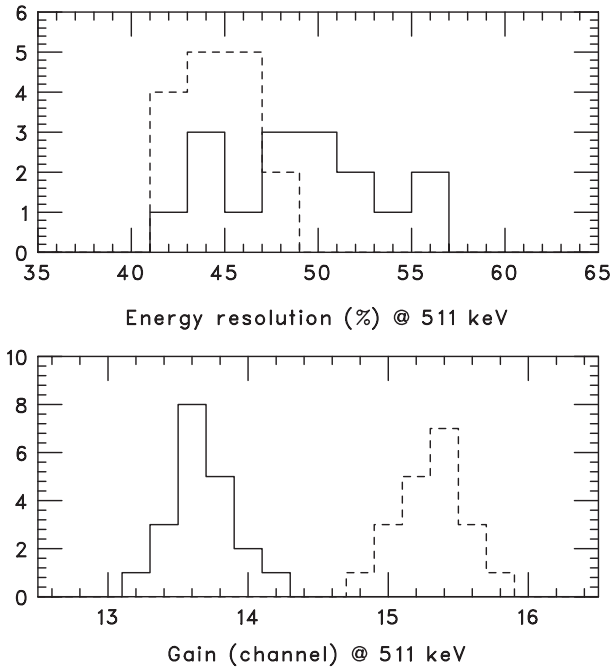

Fig. 8. Gain and energy resolution distribution of all the 16 Side units. Two plots are shown for a comparison between the early phase (2005 August 25: dashed line) and recent phase (2007 August 31: solid line).

The GRB triggering function in the AE-TPU and data readout by the DE were activated on 2005 August 22, while the DE software trigger was turned off. We first set the energy range of the TH 1 band (110–240 keV), the sample time (both 1/4 and 1 s) and the significance (8.0σ). The GRB trigger rate was found to be only 0.2 GRB candidates per day, while the total trigger rate was 1.0 per day due to high solar activity, so the level was reduced to 5.7σ to increase the GRB rate on 2006 October 31. In this operation, the DE software was also activated with the trigger to the hardware switched off to check the validity of its operation. The selected significance levels and energy channels are 5.625σ for channels 4–7 which corresponds to the AE-TPU setting. We verified that the on-board software trigger logic worked well, although the software trigger had not been turned on yet. All the current AE-TPU parameters are summarized in table 8.

3.2. *WAM Background Rejection Performance*

Background rejection is the primary role of the WAM in the HXD, and it serves this purpose very effectively. The upper panel of Figure 9 shows the HXD / PIN and GSO spectra with and without the WAM anti-coincidence during the pointed observation of the supernova remnant E0102−72 on 2007 March 17, April 10, June 13, and August 6. The WAM gain was adjusted on April 12 (table 5), which means that the energy threshold level was different by $\sim$20% between the first and last two observations. This target has often been observed for XIS calibration purposes. Hence, it is appropriate for a study of the time variability of the background.

The background rejection performance, i.e., the count rate ratio as a function of energy without anti-coincidence relative to that with anti-coincidence, is shown in the lower panel of the same figure. The background is reduced by a factor of 2. This is evident especially at the high energies of the PIN (>40 keV) and GSO (>400 keV) ranges, implying that it is not negligible. The 511 keV line due to the β^+decay of activated nuclei in the WAM is effectively rejected. The background level and rejection performance are almost the same among the four epochs,

Table 8. AE-TPU setting.

Parameter	Adjustable value	Current value
High Voltage	0–1500 V	816 to 878 V
Time mode	0,1,2,3	0 (TRN 0.5 s, BST 1/64 s)
Gain	1.0–4.0	1.7 to 2.8
LD level	6–2490 mV	128 mV ($\sim$50 keV)
Sum gain	1/2 or 1	1
Sum LD level	25–315 mV	45 mV ($\sim$30 keV)
UD level	9 V (fixed)	9 V ($\sim$5 MeV)
UD Veto width	19.2–410 μs	25.6 μs
Hit-pattern width	1.2–2.6 μs, 4.2–5.6 μs	5.6 μs
GRB judment level	5.7–16.0	5.7
GRB judment time	1/4, 1 s, or both	both 1/4 and 1 s
GRB trigger	AE-TPU, DE, or both	AE-TPU alone
RBM level	5–300 kHz	100 kHz (WAM 0,1), 10 kHz (WAM 2,3)

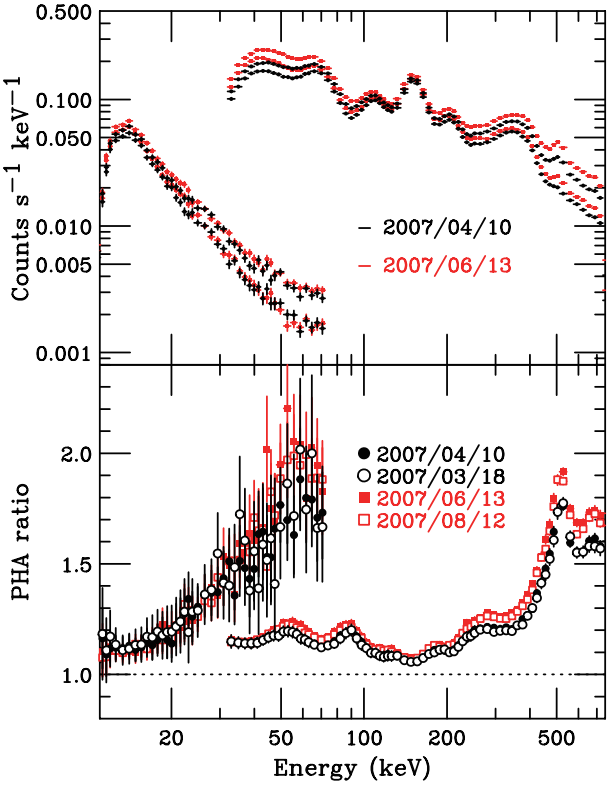

Fig. 9. Upper panel: The HXD / PIN and GSO spectra taken during pointed observations of supernova remnant E0102−72 during two epochs (red: 2007 June 13; black: 2007 April 10). The upper and lower plots correspond to spectra with and without the WAM hit-pattern. Lower panel: WAM background rejection performance during the four epochs, i.e., plotted as a count rate ratio without the WAM anti-coincidence to that with it.

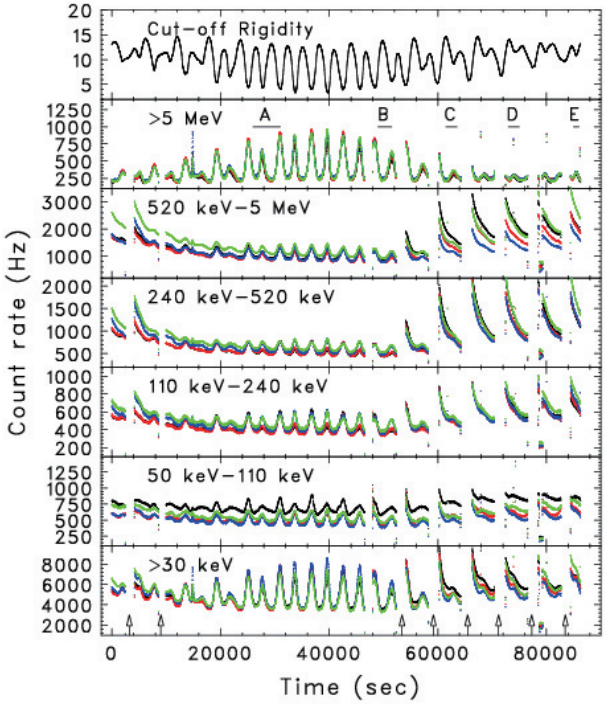

Fig. 10. Typical one-day light curves of the four WAM detectors (black:WAM 0, red:WAM 1, blue:WAM 2, green:WAM 3) in the five energy bands, together with the magnetic cutoff rigidity. The data were taken on 2006 November 15. The arrows correspond to the South Atlantic Anomaly, where the high voltage of the WAM unit is usually turned off. The WAM unit-scan operation was performed for 10 minutes at ∼79000 s.

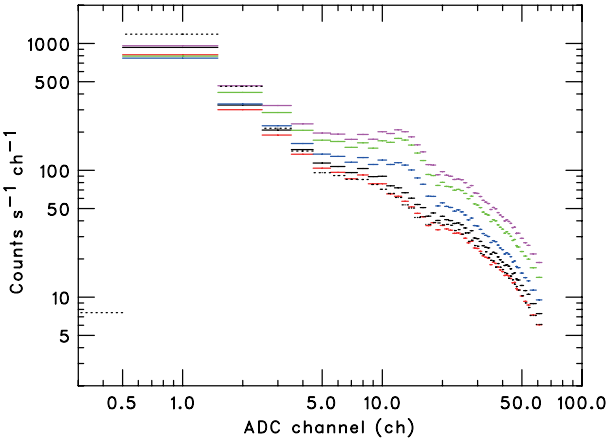

Fig. 11. WAM 3 background spectra taken on 2006 November 15. The spectra taken during epochs E, D, C, A, and B in figure 10 are shown from top to bottom. The WAM 0 spectrum during epoch A is also plotted (black dotted line). The 511 keV line due to the annihilation of positrons with electrons grows with each SAA passage.

before and after the WAM gain change. Thus, it has been verified that the background rejection performance was stable.

4. In-Orbit Background

The background of a detector in low-Earth orbit is dramatically time-variable mainly due to the geomagnetic cut-off rigidity and the SAA. A typical one-day WAM light curve is shown in figure 10. The background rate per WAM detector (four Side units) is typically 4.8 kHz in the 50–5000 keV band. In energy bands above 5 MeV, the background is dominated by high-energy particles with an energy momentum of ∼GeV/c, which penetrate into the magnetosphere. The counting rate displays modulations, especially in the non-SAA orbits, which are tightly anti-correlated with geomagnetic cut-off rigidity. It sometimes displays a flare-like behavior in only this energy band (see around 15000 s in figure 10), which corresponds to passage through the edge of the SAA region. In the intermediate energy band (240 keV–5 MeV), the counting rate increases significantly every time the satellite passes through the SAA. The exponential decay time scale after SAA passage is explained by at least two components (∼10 min and ∼3 hr). Figure 11 shows the background spectra taken near the SAA passage. It is found that the 511 keV line increases due to the annihilation of cosmic-ray generated positrons with electrons in the surrounding materials. Atmospheric gamma-rays, magnetospheric charged particles (subsection 6.1), astronomical phenomena such as solar flares (subsection 8.2) and bright hard X-ray sources (subsection 8.1) seem to be dominant in the energy range below 240 keV.

In addition to the time-variations on a time scale of one day,

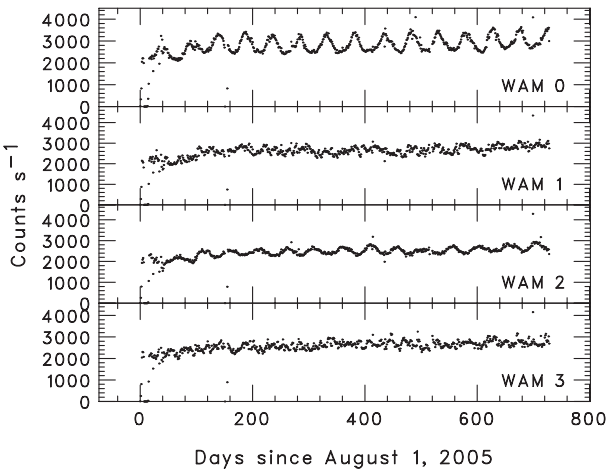

Fig. 12. Long-term behaviour of the WAM background in the 50–5000 keV range. Each point represents the averaged count rate for one-day. WAM 0 and 2 show a clear modulation with a precession period of 53 days, while WAM 1 and 3 show little variability.

long-term variations in the instrumental background are seen in the WAM light curve. Figure 12 shows one-day averaged light curves of all the detectors in the 50–5000 keV range since launch. All of the detectors show different behaviors. WAM 0 and 2 display a clear modulation with a period of 53 days which corresponds to the precession of the Suzaku satellite. The amplitude of the variation in WAM 0 is larger than that of the WAM 2, and the WAM 0 has the opposite phase with respect to WAM 2. On the other hand, no clear modulations are seen in the other two detectors, WAM 1 and 3, which only show some increase due to the activation component since launch. This modulation is very useful for background estimation.

5. Energy Response

5.1. Generation of Energy Response Matrix

We have developed an energy-response generator, *wamrspgen*, for spectral analysis (Ohno et al. 2005). The WAM response is very complicated because it is affected by the surrounding materials on the satellite, depending on the direction of incidence. The current WAM energy response as a function of incidence is calculated using the Suzaku mass model based on the GEANT4 simulation toolkit (Agostinelli et al. 2003, Ozaki et al. 2005, Terada et al. 2005, Ohno et al. 2005). This mass model has been constructed based on the spacecraft design, and further tuned by comparing both experimental data taken on the ground and in-orbit, along with Monte-Carlo simulations. The calibration sources are radio-isotopes on the ground, and GRBs, the Crab Nebula, and solar flares in orbit. The flux accuracy is now about 30% for all directions.

The method for constructing the response matrices is the following

1. 100000 photons in a parallel beam are irradiated on the Suzaku mass model from a given direction (θ, ϕ as defined in figure 3). The beam size is 70 cm × 70 cm, so as to include the entire HXD.
2. The energy deposit at each position is calculated in GEANT4. The low-energy electromagnetic package has been used.
3. The energy is converted into a pulse-height channel using the recent gain history data and the positional dependence of the light yield. Randomization is also performed based on the energy resolution at each position of each detector.
4. These procedures are repeated for 10 keV–20 MeV photons with about 300 energies on a quasi-log scale.
5. The output is converted into the FITS format (the response file), which is readable in XSPEC.

It takes ∼12 hr to complete one energy response using a PC with an Intel Pentium IV 3.2 GHz CPU. Rather than the raw ADC value (PHA), the pulse invariant (PI), i.e., gain-corrected PHA, is usually used in the energy scale in the field of X-ray astronomy. However, we do not use the PI channel due to the small number of ADC channels, so the energy responses are calculated for each GRB while taking into account the gain variations. The response generator has been revised since launch, and the current version is 1.9. The *wamrspgen* is not publicly available because of its large and complicated structure. The products for individual GRBs will be released through the Suzaku WAM web site.

5.2. Pre-Flight Calibration

Pre-flight calibration of the WAM was performed on 2004 June 28–29 before installation on the satellite, and after that on 2004 July 15. The main purposes of this calibration were 1) to understand the characteristics of each of the 20 units after detector construction, 2) to study the incident-angle dependence of the spectrum, and 3) to investigate the absorption or scattering due to the satellite materials.

First, the positional dependence of the light yield (LY) was measured using collimated gamma-rays. The 511 keV and 1274 keV gamma-ray lines from ^{22}Na were used for this measurement, and one wall was irradiated with a 1 cm × 30 cm collimated rectangle beam using lead blocks. Figure 13 shows the positional dependence of the LY along the Z-axis for 16 Side units. All of the units show similar characteristics. The LY in the "bottom" part is almost constant with position (up to 8.5 cm from the PMT surface which is a boundary of the two parts), while the LY at the "top" part increases linearly at a rate of ∼1.25% cm^{-1} as the distance from the PMT increases. This dependence is approximated by the following equations:

$$LY(x,y,z) = \begin{cases} az+b & (8.5\,\mathrm{cm} < z < 38.0\,\mathrm{cm}) \\ c & (0\,\mathrm{cm} < z < 8.5\,\mathrm{cm}). \end{cases} \quad (2)$$

The constants a, b, and c are put into the calibration data base. We also confirmed that this relation did not change before and after integration. This variation is due to the difference in the light-collection efficiency at the incident position. This does not depend strongly on the gamma-ray energy. The energy resolution also depends on the incident position, but is correlated with LY as (LY)$^{-1/2}$, which means that the resolution is dominated by the Poisson distribution of the primary electrons produced at the PMT.

The calibration for the angular response as a function of the incident angles was performed using the following radio-isotopes (RI): ^{241}Am (59.5 keV), ^{57}Co (122 keV, 136 keV),

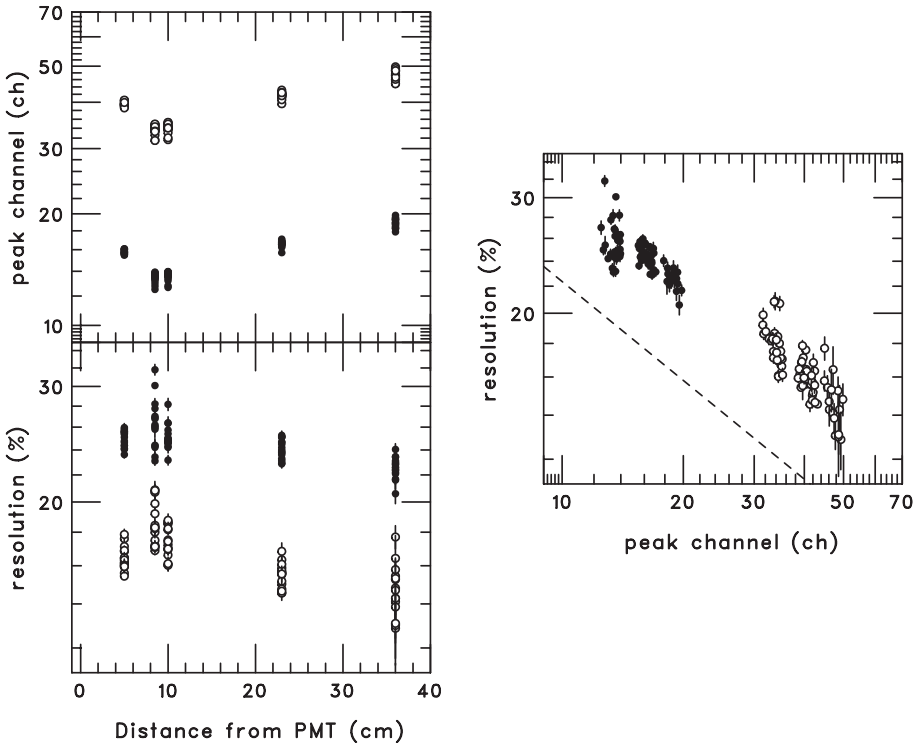

Fig. 13. Positional dependence of the peak channel and the energy resolution measured at 511 keV and 1274 keV for the 16 WAM sensors. Upper left panel: peak channels. Lower left panel: FWHM energy resolutions. Right panel: the resolution vs the peak channel. The dashed line shows inverse square root of the peak channel.

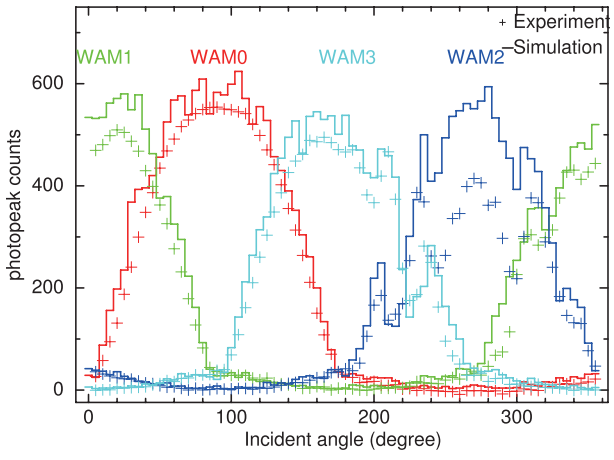

Fig. 14. Azimuth angle (ϕ) dependence of the 511 keV photo-peak count rate of the four WAM detectors on the satellite (Crosses indicate experimental results and solid lines indicate simultations). The inclination angle (θ) was fixed at 90°. The WAM 0 side is not affected much by electronics boxes and materials on the satellite, while WAM 2 is significantly affected by them.

^{133}Ba(81 keV, 356 keV), ^{137}Cs (661.6 keV), ^{22}Na (511 keV, 1274 keV) and ^{88}Y(894 keV, 1836 keV). The RIs were used without any collimation from various positions at 3 m distance from the HXD center. In an irradiation test of the HXD alone, we verified that the count rate detected in each wall varied very smoothly following the expected ideal cosine function of the azimuth angle (ϕ). No significant differences among the four walls could be seen. But, once the HXD was on the satellite, the response was distorted significantly by strong absorption due to the materials on the panel. Figure 14 shows the incident angle (ϕ) dependence of the photo-peak count rate at 511 keV from ^{22}Na, which was put at a zenith angle θ of 90°. The cleanest response was that of the WAM 0 detector, which showed little effect due to absorption, while heavy absorption was seen in the WAM 2 detector, which is located at the XRS side ($\phi = 270°$).

5.3. *In-Flight Calibration*

The WAM in-flight absolute flux calibration was performed using bright sources, such as gamma-ray bursts, the Crab Nebula, and solar flares. The Crab Nebula is the most common source for calibration of X-ray and gamma-ray instruments, because it has a well-known spectral shape and flux (Toor & Seward 1974). However, even the Crab is not bright enough for the WAM, so we had to obtain the spectrum by integrating over different observation epochs. GRBs are the most suitable targets for the WAM in-flight calibration because they are much brighter, by a factor of 100–10000, and have a much harder spectra than the Crab Nebula. Hence, we have cross-calibrated the WAM with two well-calibrated instruments, which have overlapping energy ranges: Swift/BAT in the 15–150 keV range (Gehrels et al. 2004) and Konus-Wind in the 15–10000 keV range (Aptekar et al. 1995). We have exchanged the data for 24 GRBs so far.

Figure 15 shows the light curves of the bright long-duration

GRB 051008, taken by the three instruments. This burst was discovered and localized by the Swift BAT (Marshall et al. 2005), and a refined position was found by the XRT (Perri et al. 2005). The Konus-Wind time was corrected for the time of flight between the spacecraft, and almost the same time intervals were chosen for extracting the spectra (see figure 15). The WAM response was calculated for the incident direction $(\theta, \phi) = (130, 133)$. Figure 16 shows the calculated response function for GRB 051008 at various incident photon energies. The three spectra were fitted jointly by a Band GRB function (Band et al. 1993, `grbm` in XSPEC) introducing a normalization factor among the three instruments (fixed at 1 for Konus-Wind). The WAM energy range was limited to 120–5000 keV due to calibration uncertainties at lower energies (see below), and the two WAM detectors, WAM 0 and 3, which showed strong signals in the four detectors, were used for the spectral fitting. The fits are acceptable, giving a reduced χ^2 of 180/188. The spectral parameters are $\alpha = -0.93 \pm 0.06$, $\beta = -2.64^{+0.29}_{-0.58}$, and $E_{\rm peak} = 711^{+66}_{-61}$ keV. The WAM normalization factors were found to be 0.91 ± 0.05 and 0.92 ± 0.05 for WAM 0 and 3, respectively. As can be seen in figure 17, no systematic residuals are present in this energy range, suggesting that the current WAM response well-reproduces the GRB spectrum above 100 keV.

The same procedures were carried out for other GRBs.

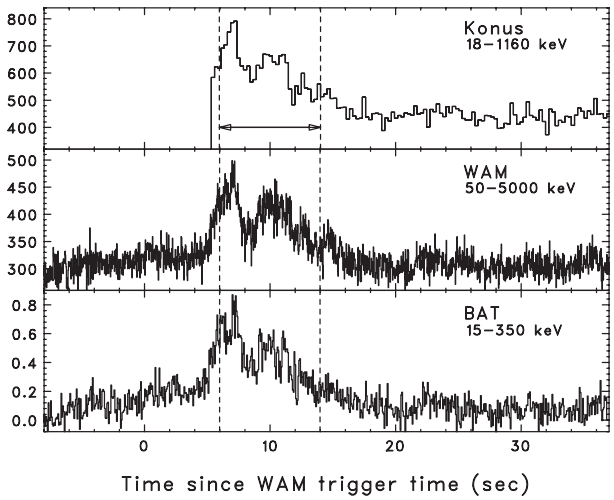

Fig. 15. Konus-Wind, Suzaku-WAM, and Swift / BAT light curves of the bright hard GRB 051008. The time of flight was corrected for. The double-headed arrow shows the integration time region for extracting the spectra.

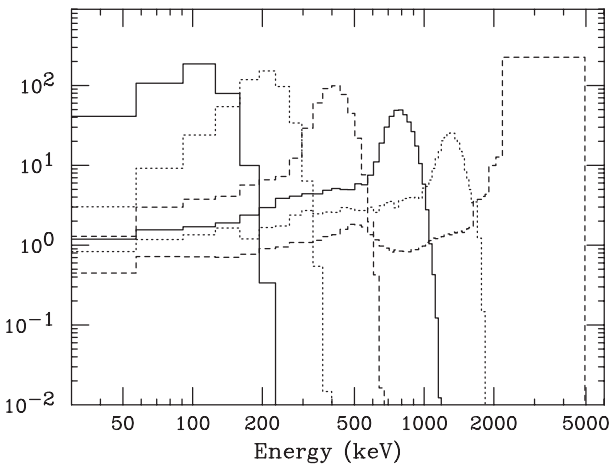

Fig. 16. Calculated response function for GRB 051008 at various photon energies.

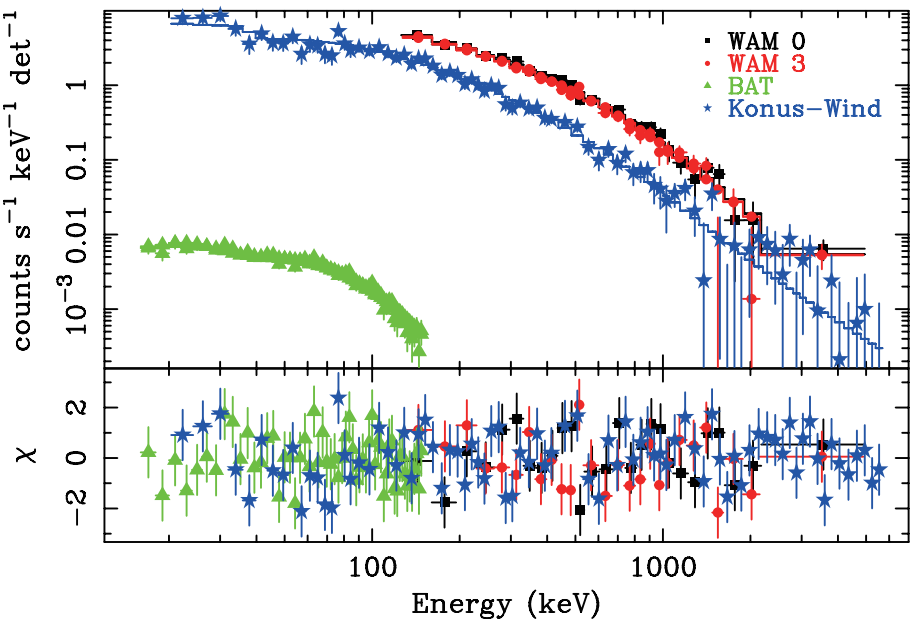

Fig. 17. Simultaneous spectral fit for GRB 051008 with Konus-Wind (blue), Suzaku-WAM (WAM 0: black and WAM 3: red), and Swift / BAT (green). The spectra are integrated over the time-region showed by the arrow (figure 15), and normalized to one detector unit for WAM and Konus or one CZT pixel for BAT. Lower panel: Residuals for the best-fit model (the Band GRB function; see subsection 3.5 for details of parameters.).

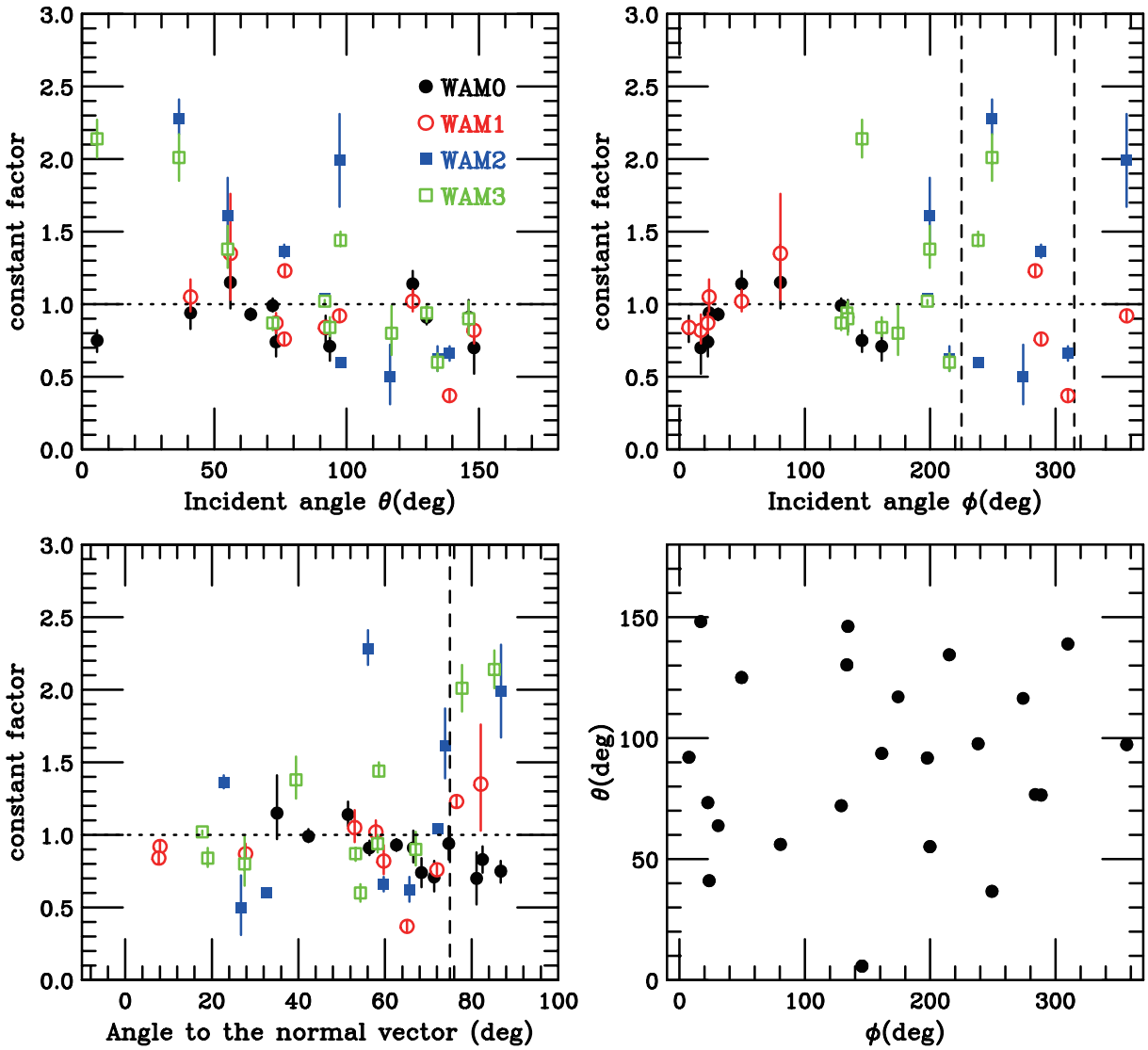

Fig. 18. Incident angle dependence of the introduced normalization factor for 21 GRBs, including GRB 051008 (upper two panels for θ and ϕ, and lower left panel for angle from normal incidence of each detector). Lower right panel: θ–ϕ distribution. The normalization factor roughly reflects the flux calibration uncertainties.

Figure 18 shows the incident angle (θ, ϕ) dependence of the normalization factor for 21 GRBs. They have an almost uniform distribution in the (θ, ϕ) plane (lower right hand panel of figure 18). The current response matrices have large flux uncertainties in some directions, such as the XRS directions (ϕ $\sim$225°–315°). and off-axis (more than 75° away from normal incidence of each detector), but the current uncertainties above 100 keV are estimated at 10%–40%. The most reliable detector is the WAM 0, which is not affected by heavy absorption. In the four energy bins (PH 0–3) with less than $\sim$120 keV, more than 40% residuals are found for all of the GRBs. This is probably due to uncertainties in the ADC baselines, the non-linearity of light output from the BGO crystals, and the absorption effects of the surrounding $BaSO_4$ and CFRP on the BGO crystals and other materials. The details of these cross-calibration results will be reported in another paper (T. Sakamoto et al. 2009, in preparation). These results were confirmed with Crab spectra taken by the Earth occultation technique.

6. GRB Detection Capability

6.1. *Trigger Status*

There have been 750 GRB triggers through August 2007, corresponding to a rate of 1 per day. Based on the durations, the shapes of the energy spectra (hardness ratio), geographic coordinates of the satellite, and simultaneous detections by other satellites, an event classification was carried out. GRBs have relatively short durations (less than 100 s), hard spectra, and a random distribution in geographic coordinates. Simultaneous detections by other satellites are also searched for in the interplanetary network (IPN) data. The SGRs have much shorter durations ($\sim$1 s) and softer spectra than those of GRBs. Solar flares always come from the direction toward the WAM 0

Table 9. Event classification of the GRB triggers (2005 Aug 22–2007 Aug 31).

Trigger significance	2005 Aug 22–2005 Oct 31 8.0σ	2005 Oct 31–2007 Aug 31 5.7σ	2005 Aug 22–2007 Aug 31 all($8.0\sigma + 5.7\sigma$)
Confirmed GRBs	9 (12.5%)	178 (26.3%)	187 (24.9%)
Possible GRBs	4 (5.6%)	91 (13.4%)	95 (12.7%)
SGRs	0 (0.0%)	5 (0.7%)	5 (0.7%)
Solar flares	17 (23.6%)	11 (1.6%)	28 (3.7%)
Particle events	30 (41.7%)	88 (13.0%)	118 (15.7%)
SAA	4 (5.6%)	6 (0.9%)	10 (1.3%)
Statistical fluctuations	0 (0.0%)	283 (41.7%)	283 (37.7%)
Others (accidental)	8 (11.1%)	14 (2.0%)	23 (3.0%)
Data lost	0 (0.0%)	2 (0.3%)	2 (0.3%)
Total	72	678	750

Table 10. Simultaneous GRB events from 2005 August 1 to 2007 August 31.

Instruments	Triggered	Untriggered	Total
Ulysses	10	2	12
MESSENGER	27	11	38
Mars-Odyssey	75	25	100
Konus-Wind	157	95	252
INTEGRAL SPI-ACS	76	24	100
Swift / BAT in FOV	35	24	59
Swift / BAT out of FOV	44	20	64
HETE-2	7	5	12
INTEGRAL IBIS	2	3	5
AGILE (superAGILE)	1	0	1
RHESSI	72	42	114
Total	187	127	314

detector, and have softer spectra than GRBs. Flares are sometimes detected by GOES and RHESSI. Particle events in the non-SAA orbits have relatively soft spectra (< 300 keV) with long durations (minutes). An increase in the count rate is seen at almost the same level in all the detectors. Their geographic coordinates are concentrated on the geomagnetic poles near North America, which have low geomagnetic cutoff rigidity. This type of event was also observed by CGRO / BATSE and interpreted as bremsstrahlung radiation from trapped charged particles (Mallozzi et al. 1993). Thus, all of the GRB triggers were classified into eight categories: GRBs confirmed by other satellites, GRB candidates detected only by the WAM, SGRs, solar flares, particle events, SAA, triggers due to statistical fluctuations or possibly short spike events, and other accidental triggers. Table 9 shows the result of the event classification. The trigger significance level was changed from 8.0σ to 5.7σ on 2007 November 1. After that, apparently featureless events, which we refer to as "noise", started to trigger the WAM. The rate for this type of event is ~ 0.4 per day, which is too many to be expected from a normal distribution (0.02 per day). In spite of these noise triggers, the confirmed GRB trigger rate increased to about 8.5 from about 3.9 per month. Further refinements of the trigger, including the software logic, may be investigated.

We have further surveyed the TRN data by searching for events which are missed by the on-board trigger, and checking them manually by eye and automatically by software. These candidate events are reported to the IPN. In total, 314 GRBs, including triggered events, were confirmed by other satellites. Table 10 gives simultaneous detection information based on the IPN GRB master list.[4] The WAM confirmed GRB rate is about 140 GRBs per year, which is one of the largest rates among the current GRB detectors.

6.2. *Trigger Efficiency and Sensitivity*

Using the Swift / BAT and WAM correlation, we can estimate the WAM sensitivity to GRBs. We first exclude the Swift GRBs that satisfied the following criteria: 1) the GRB was occulted by the Earth and 2) Suzaku was in the SAA. For the remaining 112 Swift / BAT GRBs, we investigated whether they were detected or not by the WAM. 57 GRBs were detected with the WAM, and of which 31 were triggered. The WAM spectral parameters for 28 GRBs, such as GRB 051008, GRB 051111, and GRB 051221, have already been reported in GCN circulars. Swift / BAT by itself can not determine the peak energy, $E_{\rm peak}$, in some cases, but a combination of Swift / BAT and Suzaku / WAM can determine the $E_{\rm peak}$ for almost all of the triggered bursts (H. A. Krimm et al. 2009, in preparation). The upper panel of figure 19 shows the detection and trigger efficiencies for the WAM derived using Swift bursts. The lower panel of figure 19 shows the integral log N–log P distributions of the Swift / GRBs and the WAM / GRBs. The Swift 15–150 keV peak flux data were collected from published GCN circulars. The detection and trigger levels for a 1-s integration are estimated to be ~ 1.0 and 3.0 photons $\mathrm{cm^{-2}s^{-1}}$ in the 15–150 keV range. Assuming the photon index derived by the BAT, we also estimated them to be 0.5 and 1.0 photons $\mathrm{cm^{-2}s^{-1}}$ in the 50–300 keV energy range, which is worse than that of BATSE (0.2 photons $\mathrm{cm^{-2}s^{-1}}$), but comparable to that of Fermi / GBM (0.71 photons $\mathrm{cm^{-2}s^{-1}}$), probably due to a lack of WAM low-energy sensitivity.

The 110–240 keV (= nominal trigger band: TH1) WAM background rate for one WAM and the 50–300 keV rate are 0.6 kHz and 1.0 kHz, respectively. Taking into account the

[4] ⟨http://ssl.berkeley.edu/ipn3/index.html⟩.

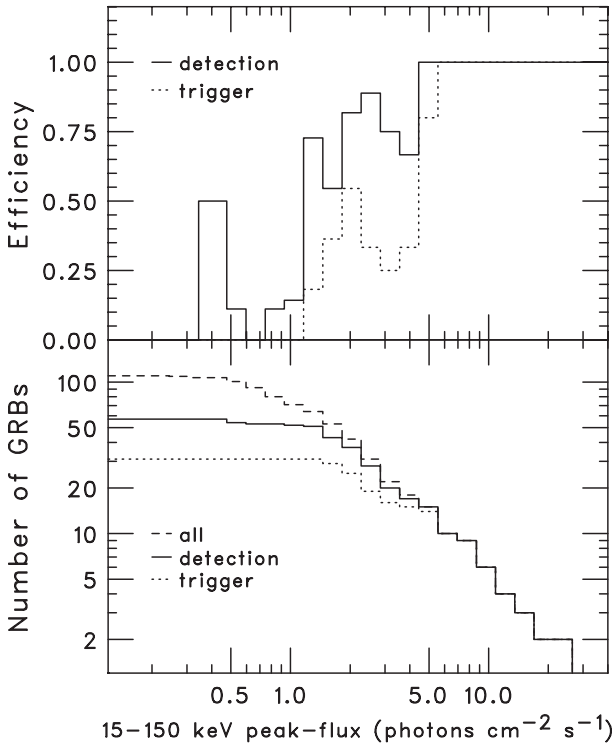

Fig. 19. Upper panel: Trigger and detection effciencies based on Swift GRBs. Lower panel: Log N–log P distribution for 112 Swift GRBs which were visible for the Suzaku WAM. The dotted lines show all of the data, while the solid lines show the bursts that the WAM could actually detect.

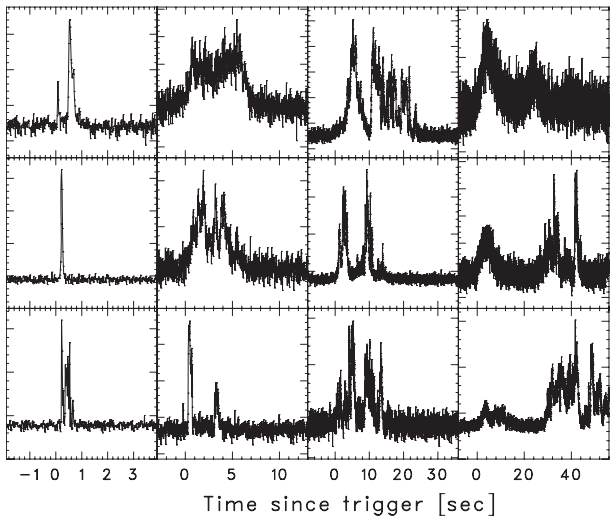

Fig. 20. Examples of GRB light curves in the 50–5000 keV range. This is produced using the BST data with a fine time resolution (1/64 s). The light curves show a variety of variations with short and long durations.

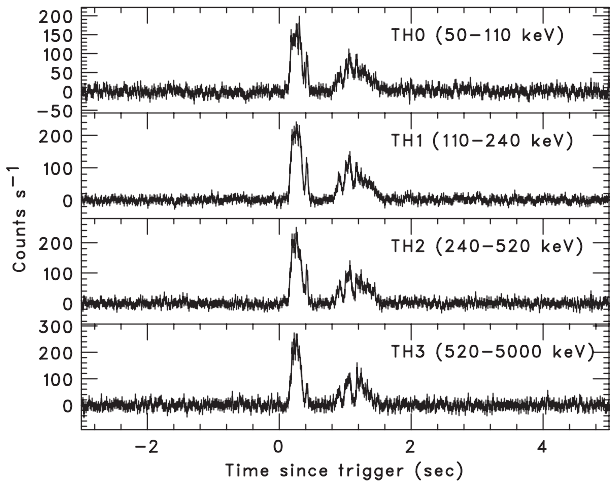

Fig. 21. Example of the short-duration GRB 060317 in the four TH energy bands. High-quality light curves can be obtained even in the highest energy band (> 520 keV).

effective area averaged over all angles ($S \sim 300$–$400\,\mathrm{cm}^2$), we can calculate the detection sensitivity using the equation: $F_{\mathrm{det}} = \sigma\sqrt{B}/S$, where B is the background rate, S is the effective area, and $\sigma = 5.7$. The derived sensitivity is 0.5–0.6 photons $\mathrm{cm}^{-2}\mathrm{s}^{-1}$ in the 50–300 keV band, which is consistent with the above results. Taking the BATSE peak fluxes from the revised 4th catalog (Paciesas et al. 1999) and the WAM sky coverage (about half the sky), the expected GRB trigger rate is ~ 100 per year, which is almost consistent with our observed trigger rate.

6.3. *Light Curves and Durations*

Some examples of WAM GRB light curves with 1/64 s resolution extracted from the BST data are shown in figure 20.

They show a variety of variations with short to long durations, and with single FRED (Fast-Rise Exponential Decay)-like structures or multiple spikes. The light curves for confirmed GRBs in the four energy bands are available at the Suzaku-WAM web site.[5] When there is no trigger, only TRN data with 1 s resolution are available. These data are also made publicly available at the same site as the untriggered events.

Figure 21 shows the light curve of the short-duration GRB 060317 in the four TH bands with 1/32 s resolution. This GRB has a peak flux of 41 ± 4 photons $\mathrm{cm}^{-2}\,\mathrm{s}^{-1}$ in the 50–5000 keV range, and a very hard spectrum with $E_{\mathrm{peak}} \sim 2$ MeV (Ohno et al. 2008). Ohno et al. (2008) also estimated a lag between the 50–110 keV band and the other three bands (110-240 keV, 240-520 keV, and 520–5000 keV), and found that all were consistent with zero, indicating that this GRB indeed belongs to the short-burst category. Thus, the WAM can produce high-quality data for variability studies, even in the highest energy range above 520 keV, owing to its large effective area.

The T90 duration distribution for triggered bursts is shown in figure 22. We have plotted it for confirmed GRBs and possible GRBs. The T90 duration was calculated as the time interval starting after 5% and ending after 95% of the counts in the 50–5000 keV range. The distribution of the BATSE sample in the 4th revised catalog (Paciesas et al. 1999) is also shown for

[5] ⟨http://www.astro.isas.jaxa.jp/suzaku/HXD-WAM/WAM-GRB/⟩.

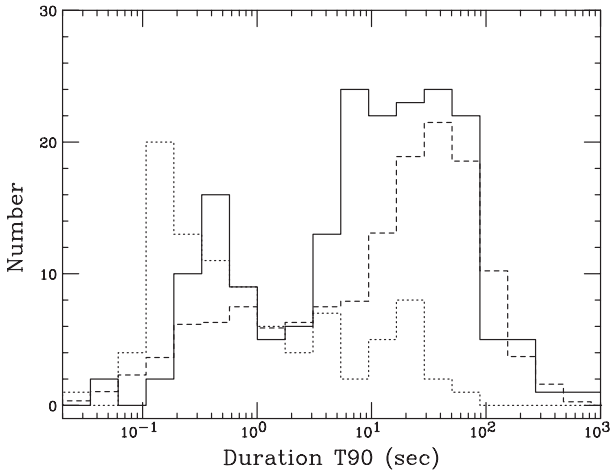

Fig. 22. T90 duration distribution of the WAM GRBs. Confirmed and possible GRBs are shown separately as solid and dotted lines, respectively. They are also compared with the BATSE GRB sample (dashed line) with arbitrary normalization.

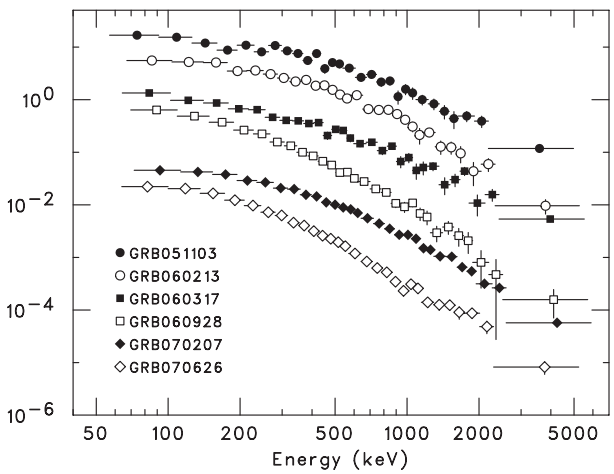

Fig. 23. Examples of WAM count spectra for six bright GRBs. GRB 051103 and GRB 060317 are classified as short-duration bursts. The largest energy bin, 2–5 MeV, corresponds to the overflow bit in the flash ADC.

a comparison. We clearly observe a bimodal distribution for confirmed GRBs which peaks at 0.2 s and 10 s. This is almost consistent with the BATSE sample, but is quite different from the Swift distribution, which has relatively few short-duration GRBs (<2 s) (Sakamoto et al. 2008). On the other hand, the distribution of possible GRBs has a very different shape from the confirmed one: there are more short-duration events in it. These short events could be terrestrial gamma-ray flashes (TGFs), particle shower events, or real short-duration GRBs, which have such weak intensities that they cannot be detected by other instruments.

6.4. Energy Spectra

An important feature of the WAM is its large effective area in the MeV range. Figure 23 shows time-averaged spectra in raw detector counts for six bright GRBs, which were localized by the IPN. This sample includes two short GRBs: GRB 051103 and GRB 060317. All the bursts (even the short bursts) show clear signals above 1 MeV. High-quality spectra can be obtained up to $\sim$5 MeV. This capability is a very powerful tool for determining the high-energy photon index, β, and studying the connection between the low-energy component, presumably due to synchrotron emission, and the poorly understood high-energy component ($>$ MeV) detected by EGRET / TASC (Gonzalez et al. 2003), which might be detected by Fermi and AGILE.

7. GRB Localization

7.1. IPN Localization

There are two ways to localize GRBs with wide-field instruments which do not have imaging optics, such as the coded masks utilized by Swift / BAT and INTEGRAL IBIS. The first one is triangulation using interplanetary spacecraft, the IPN techinique. The GRB direction (θ) depends on the arrival time difference (Δt) and the satellite distance (D), so we can constrain the direction to an annulus with the following uncertainty in $\Delta\theta$:

$$\Delta\theta = \frac{c\Delta t}{D\sin\theta}, \tag{3}$$

where Δt is measured by cross-correlating the time histories taken in comparable energy bands. Four non-coplanar instruments yield a single error box. If we have detections by only three instruments, we can derive two GRB error boxes where the two annuli intersect. Further criteria, such as Earth occultations or coarse directional information, can eliminate one of them. This method is capable of $\sim$arcminute accuracies, which is comparable with Swift / BAT, and allows follow-up observations by the Swift XRT with a FOV of $20' \times 20'$.

Millisecond accuracy of the WAM absolute timing is essential in localizing GRBs by this method. It has been checked by cross-correlating the Suzaku WAM time histories with Konus-Wind, RHESSI, and Swift / BAT using well-localized GRBs and SGRs. Table 11 shows a list of 15 Swift GRBs localized by the Swift XRT or optical telescopes. The measured time delays between Swift / BAT and Suzaku-WAM were compared with the expected one. Only data that have good statistics have been selected. If we average the difference between the predicted and measured time delays for the ensemble of 15 bursts, we obtain 0 ± 111 ms. If instead we restrict the analysis to three bursts with a chi-squared per degree of freedom of less than about 1, we obtain -2 ± 36 ms. We conclude that the Suzaku-WAM timing is consistent with negligible systematic uncertainties, as far as gamma-ray burst triangulation is concerned.[6]

Shortly after launch, the Suzaku WAM joined the third IPN, which at the time consisted of Ulysses, MESSENGER, Mars-Odyssey, Konus-Wind, INTEGRAL, RHESSI, AGILE, HETE-2, and Swift (Ulysses and HETE-2 have since ceased operations). The former three are key instruments, because they are in interplanetary space at 0.5–6 AU from the Earth. The latter four detectors are in low-Earth orbits. The Suzaku WAM has actually played an important role as one of the

[6] The timing of the HXD main detector was already verified using the Crab pulsar to 360 μs (Terada et al. 2008).

Table 11. Timing verification results using 15 Swift GRBs.

GRB name	Predicted (s)	Measured (s)	Difference (sigma)	χ^2/d.o.f
GRB 051008	0.023	-0.041 ± 0.036	0.064 (1.78)	2.13
GRB 051221	0.009	0.004 ± 0.001	0.005 (5.00)	3.17
GRB 060105	−0.021	-0.021 ± 0.004	−0.006 (1.50)	4.25
GRB 060117	−0.016	-0.020 ± 0.007	0.004 (0.57)	1.12
GRB 060306	−0.012	-0.010 ± 0.030	−0.002 (0.07)	0.81
GRB 060801	0.001	-0.010 ± 0.018	−0.008 (0.44)	1.03
GRB 060813	0.004	0.000 ± 0.032	0.004 (0.13)	1.59
GRB 060814	−0.001	0.041 ± 0.086	−0.042 (0.49)	3.83
GRB 060904	−0.002	-0.022 ± 0.010	0.020 (2.00)	2.62
GRB 060912	0.004	-0.096 ± 0.027	0.100 (3.70)	2.13
GRB 061006	−0.013	-0.016 ± 0.002	0.003 (1.50)	3.33
GRB 061007	0.001	0.023 ± 0.003	−0.022 (7.33)	9.15
GRB 061210	−0.015	-0.009 ± 0.002	−0.006 (3.00)	4.57
GRB 061222	−0.019	-0.004 ± 0.005	−0.015 (3.00)	3.40
GRB 070328	0.003	0.104 ± 0.021	−0.101 (4.81)	2.06

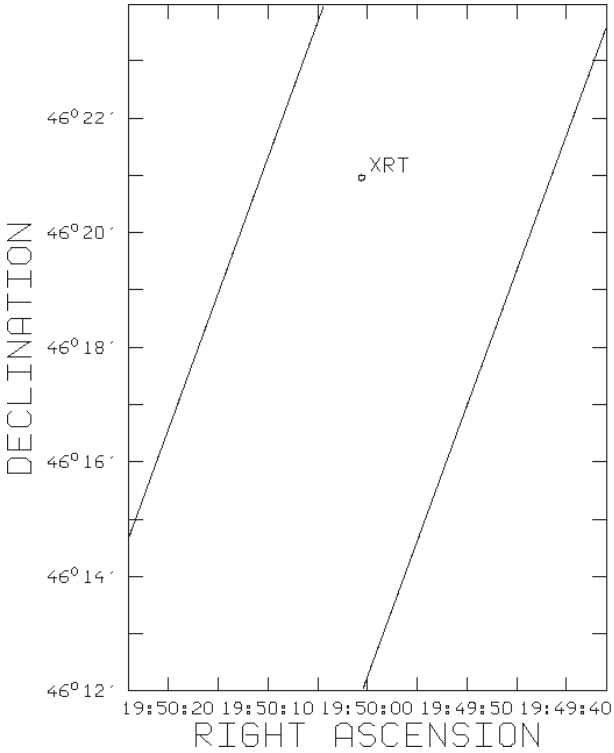

Fig. 24. Suzaku-Mars Odyssey triangulation of Swift GRB 060105. The IPN annulus is consistent with the XRT position indicated with a circle (Godet et al. 2006).

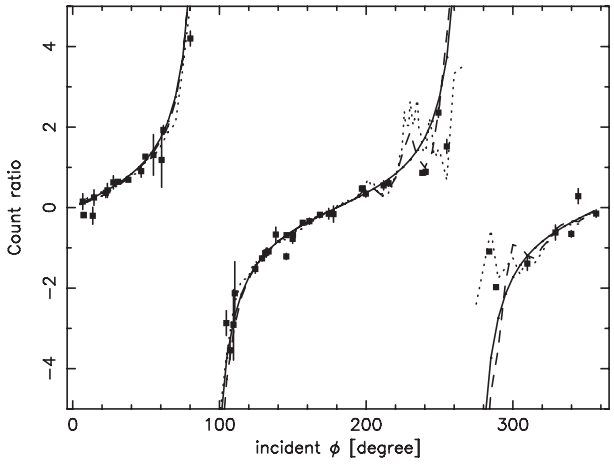

Fig. 25. Incident azimuth angle ϕ dependence of the WAM counting rate ratio in the two detectors for 51 GRBs (filled squares) with well–known postions. The solid line shows tanϕ, as expected from simple plane approximations, and the dashed and dotted line show the experimental and simulation data, respectively.

fourth instruments. The current IPN detection rate is about 200 events per year, and about a half of them are detected with the WAM. Because of its large area and high detection efficiency, the WAM is a very sensitive detector, and it records many bursts with excellent statistics. The Suzaku WAM has contributed 11 rapid localizations up to now. Figure 24 shows the Suzaku-Mars Odyssey triangulation annulus for the Swift GRB 060105. Suzaku and Odyssey were separated by 405 light-seconds, and triangulation resulted in a 4.′7 wide annulus, which includes the Swift XRT counterpart position (Godet et al. 2006).

7.2. *Localization by Relative Count Rates in the WAM Detectors*

This is the second method that can be used to localize bursts over a wide field of view. The WAM has the ability to localize GRBs using the differences between the count rates detected in the four perpendicular WAM walls; this is a similar technique to CGRO / BATSE and Fermi / GBM. The accuracy of this method is not fine enough for counterpart searches (5°–10°), but it is useful to distinguish between two error boxes obtained by the IPN, and good enough to perform spectral analysis. We have investigated this capability using 51 GRBs that had well-determined positions from Swift, HETE-2, and the IPN.

The GRB total counts are calculated above 200 keV by subtracting the model background. Figure 25 shows the count rate ratio in two detectors as a function of the GRB incident angle (ϕ). The data were also compared with Monte-Carlo simulations and RI-irradiation test results. The count rate ratio, R, should obey $R = \tan\phi$ if 1) the walls can be regarded as thin plates and 2) absorbing materials can be neglected. Almost of all of the data follow this relation, except for angles ϕ (220°–320°) that intersect complex satellite structures. This simple method can give a constraint on the azimuth angle with an accuracy of 5°. A method to constrain the zenith angle θ is under investigation. As shown in table 10, many WAM GRBs have been detected by IPN detectors, so a combination of the WAM and IPN constraints give at least a coarse position for the GRBs.

8. Other Source Detections

8.1. Hard X-Ray Source Detection by Earth Occultation Techniques

Bright hard X-ray sources with an intensity of ~ 1 Crab can be monitored by the WAM using Earth occultation methods developed by the CGRO / BATSE team (Harmon et al. 2002; Zhang et al. 1993). This method measures the step in the flux contribution when the source rises above and sets below the Earth horizon. The WAM is an ideal detector for this purpose because its FOV is not limited. The current all-sky monitors are the RXTE / ASM, which operates in the 1.5–12 keV band (Levine et al. 1996) and the Swift / BAT in the 15–50 keV range (Krimm et al. 2006), so the WAM can provide unique opportunities to monitor sources in the range above 50 keV to fill the high-energy end.

We have searched for the contributions from known sources expected at specific times based on the Suzaku orbital elements. Figure 26 shows the Earth-occultation step for the Crab Nebula. This was obtained by summing 16 orbits with the same satellite attitude. We could clearly detect signals up to 700 keV. In addition to bright X-ray binaries, such as Cygnus X-1 and GRS 1915+105, weak sources such as the radio galaxy Cen-A and the Seyfert galaxy NGC 4151 have been detected with the WAM. Giant flares from Cygnus X-1 were detected in the Earth occultation step on 2007 August 7–8, and reported in a GCN circular (Golenetskii et al. 2007). The sensitivity is estimated to be at about 500 mCrab and 30 mCrab in the 50–300 keV range for integrations of one-day and two-years, respectively. These results will be publicly available and reported in a forthcoming paper.

8.2. Soft Gamma-Ray Repeaters (SGRs) and Solar Flares

The SGRs are believed to be pulsars with strong magnetic fields (10^{14}–10^{15} G). Many short flares from the SGRs have been detected with the WAM; however, most of the events did not trigger, due to their soft spectra (< 100 keV). Figure 27 shows a 50–240 keV light curve of the SGR intermediate flare at 14:25:01.387 on 2006 August 6. This event triggered the WAM due to its brightness. The T90 duration was ~ 26 s, and the fluence measured by Konus-Wind was 2.4×10^{-4} ergs cm^{-2} (Golenetskii et al. 2006). It was also observed by various other

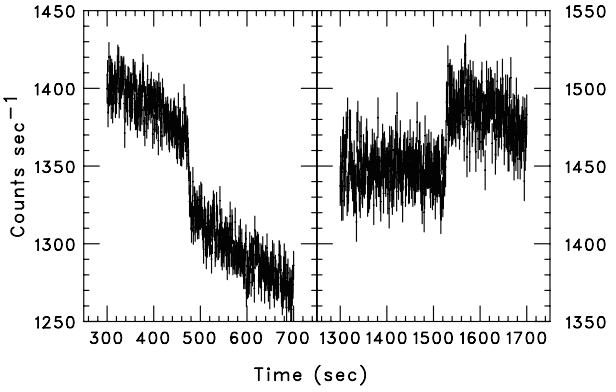

Fig. 26. Earth occultation step for the Crab observed by WAM 0 in the 50–300 keV range for 1 day integration. Crab set (Left) and Crab rise (Right).

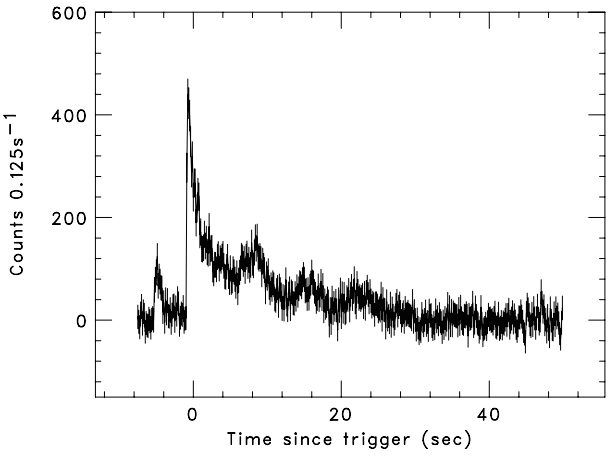

Fig. 27. WAM light curve of the intermediate flare from SGR 1806−20 on 2006 August 6 in the 50–240 keV range. The trigger time was 14:25:1.387. A 7.5 period is clearly found in this light curve.

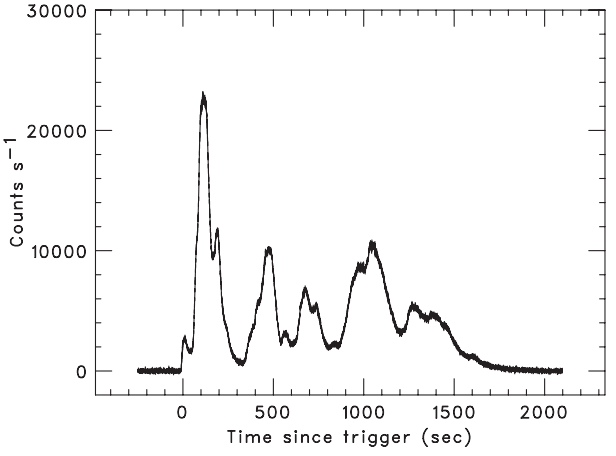

Fig. 28. WAM light curve of the solar flare on 2006 December 6. The trigger time was 19:15:36 (UT). This flare was observed by the GOES satellite as X 6.5 class.

satellites (Ulysses and Mars-Odyssey), and localized by the IPN to a position consistent with SGR 1806−20 (Hurley et al. 2006a), although it was initially reported as a long GRB due to its long duration (Hurley et al. 2006b). The WAM light curve shows a clear ~ 7.5 s pulsation, as reported in previous observations (Kouveliotou et al. 1998; Woods et al. 2007). This non-thermal high-energy radiation will be studied using WAM data.

WAM has detected 160 solar flare candidates so far. They always come from the solar paddle direction, i.e., the WAM 0 side. This direction is not much affected by absorbing materials (see subsection 2.1), which allows us to study the hard X-ray emission without calibration uncertainties. Figure 28 shows a WAM 0 light curve with 1 s resolution for an X6.5 class solar flare. This flare triggered the WAM at 19:15:36 on 2005 December 6. The T90 duration was 1350 s, so the BST data cannot cover the entire flare. We could succesfully obtain the whole light curve with no loss of data due to RBM activation, although the event deadtime was significant.

9. Summary and Conclutions

We have presented the design and the in-orbit performance of the Suzaku Wide-band All-sky Monitor (WAM), which utilizes the anti-coincidence shield of the Hard X-ray Detector (HXD). The 20 BGO sensors and their electronics have been operating nominally since launch. WAM energy calibration has been performed using GRBs simultaneously detected by other satellites. The current flux uncertainties are estimated to be less than 40% above 100 keV, except for some directions. Work is in progress to improve this. The absolute timing accuracy of the satellite clock has been verified, and the WAM has been added to the interplanetary network as a detector in low-Earth orbit. WAM has already detected 314 GRBs in over two years of operation, corresponding to 140 GRBs per year. Thus, WAM has established itself as the fourth instrument in the Suzaku mission.

The Suzaku program, and thus the HXD instrument, were supported by ISAS/JAXA and NASA. This research has been supported in part by a Grant-in-Aid for Scientific Research (17030008, 19047001 KY and 20041001 ST) of the Ministry of Education, Culture, Sports, Science and Technology (MEXT). KH is grateful for support under the NASA Suzaku Guest Investigation Program, grants NNX06AI36G and NNX08AB84G.

References

Agostinelli, S., et al. 2003, Nucl. Instrum. Methods Phys. Res., A, 506, 250
Aptekar, R. L., et al. 1995, Space Science Reviews 71, 265
Band, D., et al. 1993, ApJ, 413, 281
Feroci, M., et al. 1997, Proc. SPIE, 3114, 186
Fishman, G. J., et al. 1994, Science, 264, 1313
Gehrels, N., et al. 2004, ApJ, 611, 1005
Godet, O., et al. 2006, GCN Circ., 4433
Golenetskii, S., et al. 2007, GCN Circ., 6745
Golenetskii, S., Frederiks, D., Pal'shin, V., Aptekar, R., Cline, T., & Mazets, E. 2006, GCN Circ., 5426
Gonzalez, M. M, Dingus, B. L., Kaneko, Y., Preece, R. D., Dermer, C. D., & Briggs, M. S. 2003, Nature, 424, 749
Harmon, B. A., et al. 2002, ApJS, 138, 149
Hurley, K., et al. 2006a, GCN Circ., 5416
Hurley, K., et al. 2006b, GCN Circ., 5419
Kelley, R. L., et al. 2007, PASJ, 59, S77
Kokubun, M., et al. 2007, PASJ, 59, S53
Kouveliotou, C., et al. 1998, Nature, 393, 235
Koyama, K., et al. 2007, PASJ, 59, S23
Krimm, H. A., et al. 2006, ATEL, 904
Levine, A. M., Bradt, H., Cui, W., Jernigan, J. G., Morgan, E. H., Remillard, R., Shirey, R. E., & Smith, D. A. 1996, ApJ 469, L33
Mallozzi, R. S., Paciesas, W. S., Meegan, C. A., Fishman, G. J., Wilson, R. B. 1993, AIP Conf. Proc., 280, 1122
Marshall, F., Barthelmy, S., Cummings, J., Norris, J., Perri, M., & Sakamoto, T. 2005, GCN Circ., 4069
Mitsuda, K., et al. 2007, PASJ, 59, S1
Ohno, M., et al. 2005, IEEE Trans. Nucl. Sci., 52, 2758
Ohno, M., et al. 2008, PASJ, 60, S361
Ozaki, M., et al. 2005, IEEE Trans. Nucl. Sci., 52, 2765
Paciesas, W. S., et al. 1999, ApJS, 122, 465
Paciesas, W. S., Harmon, B. A., Fishman, G. J., Zhang, S. N., & Robinson, C. R. 1996, IAU Circ., 6284
Perri, M., Capalbi, M., & Burrows, D. N. 2005, GCN Circ., 4073
Sakamoto, T., et al. 2008, ApJS, 175, 179
Serlemitsos, P. J., et al. 2007, PASJ, 59, S9
Takahashi, T., et al. 2007, PASJ, 59, S35
Terada, Y., et al. 2005, IEEE Trans. Nucl. Sci., 52, 902
Terada, Y., et al. 2008, PASJ, 60, S25
Toor, A., & Seward, F. D. 1974, AJ, 79, 995
von Kienlin, A., et al. 2003, A&A, 411, L299
Woods, P. M., Kouveliotou, C., Finger, M. H., Göğüş, E., Wilson, C. A., Patel, S. K., Hurley, K., & Swank, J. H. 2007, ApJ, 654, 470
Yamaoka, K., et al. 2005, IEEE Trans. Nucl. Sci., 52, 2765
Yamaoka, K., et al. 2006, Proc. SPIE, 6266, 626643
Zhang, S. N., Fishman, G. J., Harmon, B. A., Paciesas, W. S. 1993, Nature, 366, 245